# Synergistic Regulation of Superconductivity by Electron Localization and Phonon Frequency partition in Endohedral Carbon Cage Compounds $XC_{20}$

Pei-Yun Xu（胥佩云）[a], Qi-Jun Liu （刘其军）[a,1]

[a] Bond and Band Engineering Group, School of Physical Science and Technology, Southwest Jiaotong University, Chengdu 610031, China

Correspondence about the paper at the following e-mail address:

Qi-Jun Liu, E-mail: qijunliu@home.swjtu.edu.cn

[1] E-mail: qijunliu@home.swjtu.edu.cn

Abstract: In this work, we employ first-principles calculations and take the $C_{20}$ carbon cage covalent framework as the research system to systematically investigate the modulation effect of different endohedral atoms X on the electron–phonon coupling (EPC) strength and superconducting transition temperature $T_C$ of $XC_{20}$ compounds. We focus on elucidating the microscopic physical mechanism for the remarkable differences in superconducting properties within the identical carbon cage skeleton. Our results demonstrate that endohedral atoms exert synergistic modulation from two dimensions: electronic structure and phonon spectrum. On the electronic side, the charge transfer effect simultaneously modulates both the density of states at the Fermi level $N(E_F)$ and the degree of spatial localization of Fermi-level electrons, which determines the electronic baseline strength of EPC. On the phonon side, the characteristic vibrational frequency of endohedral atoms is jointly determined by atomic mass and binding strength, and low-frequency localized vibrational modes can participate in the EPC process more efficiently. The degree of synergistic matching between the two sides ultimately determines the $T_C$ of the systems. Among them, $ClC_{20}$ and $PC_{20}$ achieve the highest $T_C$ values of 29.6 K and 19.8 K, respectively. This work reveals the superconductivity modulation rule of endohedrally doped carbon cage systems, and provides theoretical support for the design of ambient-pressure carbon-based superconducting materials.

Keywords: Superconductivity; First-principles calculations; Endohedral carbon ca

ge compounds; Electron-phonon coupling; Electron localization

PACS: 74.20.-z, 71.38.-k, 61.48.-c

## 1. Introduction

Since the discovery of superconductivity, the search for superconducting materials with higher critical temperatures ($T_C$) that are stable at ambient pressure has been one of the core research topics in condensed matter physics. Although cuprate high-temperature superconductors have exceeded the liquid-nitrogen temperature barrier, a unified theoretical framework for their unconventional superconducting mechanism remains lacking, and substantial limitations persist in their synthesis and large-scale application [1-3]. In recent years, hydride superconductors have realized near-room-temperature superconductivity via strong electron–phonon coupling; however, their stable existence typically requires extreme pressures on the order of hundreds of gigapascals, which greatly limits their practical applications [4-8]. Some binary nitrides and phosphides likewise exhibit stability only under high pressure [9-12]. Accordingly, developing conventional superconducting systems that are stable at ambient pressure and exhibit a relatively high $T_C$ has emerged as a key breakthrough direction in current superconducting material research.

Among numerous candidate materials, covalent framework systems composed of the light element carbon hold unique research value: their low atomic mass yields high characteristic phonon frequencies, strong covalent bonding enables substantial electron–phonon coupling strength, and such systems are expected to maintain dynamical stability at ambient pressure, thus eliminating the reliance on extreme

pressures required for hydride superconductors. Research into superconductivity in carbon-based materials has been conducted for decades: alkali-metal-doped fullerenes $A_3C_{60}$ represent one of the earliest extensively studied carbon-based superconducting systems, with $T_C$ reaching 30–40 K. Their superconducting state lies in close proximity to a Mott insulating state, and the evolution of the critical temperature is co-determined by the lattice packing pattern, the strength of electron correlation, and the degree of molecular orientational order [13]. Subsequently, boron-doped diamond [14, 15], graphite intercalation compounds [16, 17], and other systems were likewise confirmed to exhibit superconducting transitions, but their overall $T_C$ remains below 40 K and has yet to break the temperature bottleneck of conventional superconductors. The exploration of new carbon-based superconducting materials has accordingly emerged as one of the prominent research hotspots in the field. Recent theoretical studies have successively predicted a variety of three-dimensional $sp^3$-hybridized carbon cage crystal structures, including perovskite-type $C_6$ and $LaH_{10}$-type $C_{10}$ [18]. Among these structures, studies have demonstrated that $NaC_6$ exhibits a superconducting transition temperature above 80 K at the relatively moderate pressure of 20 GPa [19]. Han et al. demonstrated that by modulating the Fermi surface position via hole doping, the superconducting $T_C$ of the $C_{10}$ carbon cage at ambient pressure is expected to exceed 100 K, while the material simultaneously exhibits superhard properties, fully verifying the superconducting potential of pure carbon cage systems [18]. As a complement to such light-element systems, research into boron-carbon (B–

C) cage compounds has likewise made corresponding advances. Related reports on $SrB_3C_3$ [20, 21], $Rb_{0.5}Sr_{0.5}B_3C_3$ [22], $XYB_6C_6$ [23], and other systems further confirm the universality of light-element covalent cage structures as hosts for ambient-pressure superconductivity.

Addressing the current research gap in endohedrally doped carbon cage superconducting systems, this work takes the reported $C_{20}$ carbon cage topological structure as the parent framework. We select nine elements as endohedral guests to construct a series of endohedral carbon cage compounds with the general formula $XC_{20}$. The selected endohedral elements are Li, Na, Mg, Al, Si, P, Cl, Sr, and Ba. Based on first-principles density functional theory calculations, we systematically investigate the structural stability, electronic structure, and superconducting properties of this series of compounds at ambient pressure. This work focuses on revealing the microscopic physical mechanism for the remarkable differences in electron–phonon coupling (EPC) and superconducting transition temperature $T_C$ induced by different endohedral atoms within the identical carbon cage skeleton. On the electronic side, the Fermi-level density of states and electron spatial localization jointly determine the electronic baseline of EPC. On the phonon side, the mass and bonding strength of endohedral atoms modulate their characteristic vibrational frequencies. Low-frequency vibrational modes dominate the contribution to EPC. The degree of synergistic matching between the electronic structure and phonon spectrum ultimately determines the superconducting $T_C$ of the system. This work clarifies the

two-dimensional synergistic modulation rule of superconducting properties in endohedral carbon cage systems. It provides theoretical reference for the atomic-level design and performance optimization of ambient-pressure carbon-based superconducting materials.

## 2.Computational Methods

All first-principles calculations were performed within the framework of density functional theory (DFT) using the Quantum ESPRESSO software package [24]. The calculations performed in this work encompass crystal structure optimization, lattice dynamics (phonon dispersion) analysis, electronic band structure calculation, and electron–phonon coupling (EPC) strength evaluation, based on which we predict the superconducting transition temperature ($T_C$). The specific computational parameters were set as follows. The exchange-correlation effects were described using the generalized gradient approximation (GGA) in the Perdew–Burke–Ernzerhof (PBE) form [25-27]. The electron–ion interaction was described using ultrasoft pseudopotentials [28]. The plane-wave and charge density cutoff energies were set to 100 Ry and 800 Ry, respectively. A Gaussian smearing width of 0.02 Ry was employed for Brillouin zone integration. For reciprocal space sampling, a 16×16×16 k-point mesh is adopted for electronic structure calculations, while a 4×4×4 q-point mesh is used for phonon and electron–phonon coupling calculations. In structural

optimization, the total energy convergence threshold is set to $1\times10^{-8}$ Ry, and the atomic force convergence criterion is set to $1\times10^{-6}$ Ry/Bohr. Convergence tests have been carried out for all the aforementioned parameters. The Coulomb pseudopotential parameter μ* is set to 0.1 and 0.11.

## 3.Results and Discussion

### 3.1 Structural properties

The carbon cage framework adopted in this work takes the cubic-symmetric carbon structure reported by Ribeiro et al. in Physical Review B in 2006 as the parent framework[29]. Its structural stability fundamentally originates from the intrinsic bonding stability of $sp^3$-hybridized carbon (Figure 1). The $sp^3$ hybrid orbitals of carbon adopt a regular tetrahedral configuration with an equilibrium bond angle of 109.47°. The resulting C–C covalent bonds exhibit high bond energy and remarkable framework rigidity, which accounts for the excellent thermodynamic and mechanical stability of the diamond lattice. A pure diamond-type $sp^3$-hybridized carbon network consists exclusively of six-membered rings, featuring a dense structure with no internal cavities available for atomic encapsulation. In contrast, the framework employed in this work is constructed from topological building units formed by the

coupling of four-membered and six-membered rings. The six-membered rings serve as the primary structural units maintaining structural stability: their bonding environment is highly similar to the intrinsic $sp^3$ hybridization state with minimal overall bond strain, forming the stable structural matrix of the entire covalent network. The four-membered rings act as topological nodes for cavity formation, enclosing cage-like cavities with high cubic symmetry and providing confined sites for the central dopant atoms.

Building on the aforementioned carbon cage framework, we introduce dopant atoms into the central cavities and construct a series of compounds with the general formula $XC_{20}$ (X = Li, Na, Mg, Al, Si, P, Cl, Sr, Ba). We calculate the formation enthalpies of the $XC_{20}$ systems, and the results are listed in Table 1. From a thermodynamic perspective, the endohedral-doped sc-$C_{20}$ systems exhibit positive formation enthalpies relative to graphite—the thermodynamically stable elemental form of carbon. This indicates that their internal energies are higher than that of the global thermodynamic stable phase, classifying them as thermodynamically metastable phases. Nevertheless, bond angle distortions and topological strain in the three-dimensional covalent framework elevate the system's internal energy but do not directly induce structural instability [29]. Furthermore, lattice dynamical calculations reveal no imaginary frequencies for all vibrational modes across the entire Brillouin zone. This rigorously confirms that the structure corresponds to a local energy minimum on the potential energy surface, with restoring forces acting against any

infinitesimal atomic displacement, thus satisfying the criterion of lattice dynamical stability.

Table 2 summarizes the unit cell volumes and C–C bond length statistics after full structural relaxation at ambient pressure. We defined the C–C bonds shared by four- and six-membered rings as $C_1$ bonds. The C–C bonds involved exclusively in six-membered rings were defined as $C_2$ bonds. The $C_1$ bond length is slightly longer than the typical $sp^3$ C–C bond length in diamond. The $C_2$ bond length is slightly shorter than the standard bond length in diamond (1.54 Å). Nevertheless, both values are very close to the standard bond length of diamond. This constitutes one of the key reasons for the ambient-pressure stability of this structure.

For the $XC_{20}$ series of compounds, the atomic radius of the endohedral dopant is a key factor governing the unit cell volume. The compounds in Figure 1 are arranged in ascending order of atomic radius. Overall, a larger effective atomic radius induces more pronounced expansion of the carbon cage framework, and the unit cell volume increases correspondingly. However, the volume variation does not strictly follow the trend of atomic radii. For example, $ClC_{20}$ exhibits a larger unit cell volume than $LiC_{20}$, which is opposite to the size trend of their central atomic radii. This discrepancy is attributed to the significantly lower electronegativity of Li relative to Cl. Central atoms with lower electronegativity tend to transfer electrons to the carbon cage framework more readily. This charge transfer increases the electron density in the

bonding orbitals of the framework and strengthens the C–C bonding interactions. This in turn leads to bond length contraction and volume shrinkage.

### 3.2 Electronic properties

We calculated the band structure of the pristine $C_{20}$ carbon cage and modulated the electronic structure near the Fermi level by endohedrally doping atoms at the cage center. Figure 2 presents the band structures and projected densities of states near the Fermi level for $C_{20}$ and the dynamically stable $XC_{20}$ compounds at ambient pressure. The band structure panels are arranged in the order of the dopant elements in the periodic table. Analysis of the Fermi-level density of states reveals that the electronic states at the Fermi level in all systems originate predominantly from C 2p orbitals. The orbital contributions from the endohedral dopant atoms are comparatively minor.

Table 3 summarizes the results of Bader charge analysis for the $XC_{20}$ compounds. With the exception of Cl in $ClC_{20}$, which accepts electrons, all other central dopant atoms undergo electron loss. This trend in charge transfer is consistent with the relative electronegativities of the corresponding elements. This finding also corroborates the electronegativity-mediated modulation mechanism for structural parameters discussed above. This accounts for the most prominent volume anomaly observed in $ClC_{20}$.

Figure 3 displays the electron localization function (ELF) and differential charge

density (DCD) maps of the carbon cage systems. To quantitatively characterize the electron localization features and charge transfer behavior of the systems, we employ two quantitative descriptors, the electron localization function (ELF) and differential charge density (DCD), for the analysis. The ELF is a scalar field defined on the basis of electron pair probability, with its value strictly confined to the range [0, 1]. An ELF value of 1 corresponds to the limit of full electron localization, while a value of 0.5 corresponds to the delocalized limit of a uniform electron gas. The magnitude of ELF directly and quantitatively reflects the degree of electron localization at any position in space. The DCD quantitatively yields the charge redistribution during bonding via the difference between the total charge density of the system and the charge density of isolated free atoms. It directly quantifies the degree of charge accumulation and depletion in each region in units of electron number density ($e/Å^3$). Based on these quantitative descriptors, we further analyze the modulating effect of charge transfer intensity, bonding characteristics and electron localization level between endohedral atoms and the carbon cage framework on electron–phonon coupling. In the DCD maps, electron accumulation regions are predominantly localized within the carbon cage framework. This observation is corroborated by the strong electron localization in C–C bonding regions evident in the ELF maps. This confirms the presence of strong covalent C–C bonding interactions in the carbon cage framework. This constitutes a key prerequisite for the structural stability of the framework at ambient pressure. To elucidate the spatial distribution of electronic states near the Fermi level,

we performed partial charge density analysis. The integration was performed within an energy window of ±0.003 eV centered on the Fermi level. The corresponding partial charge density maps were obtained, as shown in Figure 3. The results reveal that electronic states near the Fermi surface are predominantly localized at the carbon sites where three six-membered rings intersect. Furthermore, for systems with a higher Fermi-level density of states, such as $PC_{20}$ and $ClC_{20}$, the spatial localization of their electronic states is more prominent. This result confirms that partial charge density analysis can intuitively reveal the spatial distribution characteristics of Fermi-level electronic states. This provides an electronic structural basis for further understanding the microscopic origin of electron–phonon coupling in these systems.

### 3.3 Superconducting properties

To explore the superconducting potential of these ten ambient-pressure metallic carbon cage compounds, we employed the Quantum ESPRESSO (QE) package in conjunction with the McMillan equation to calculate the superconducting transition temperature $T_C$, the logarithmically averaged phonon frequency ωlog, and the Fermi-level density of states for each system. The corresponding results are presented in Figure 4 and Table 4, respectively. The phonon spectra of all compounds exhibit no imaginary frequencies throughout the Brillouin zone, verifying their dynamical stability at ambient pressure.

Based on the distribution characteristics of the phonon density of states, the phonon states in the low-frequency region (0–10 THz) in most $XC_{20}$ systems originate predominantly from the localized vibrations of the endohedral dopant atoms. The phonon states in the mid-to-high-frequency region (>10 THz) originate predominantly from the intrinsic lattice vibrations of the carbon cage framework. The physical origin of this distribution pattern lies in two factors: the extremely high force constants of C–C covalent bonds and the relatively low mass of carbon atoms. Accordingly, the intrinsic vibrations of the carbon cage framework exhibit higher characteristic frequencies. The characteristic vibrational frequencies of endohedral atoms in the confined cavity environment are typically much lower than those of the carbon framework. Remarkably, the characteristic vibrational modes of the endohedral atoms in $LiC_{20}$ and $MgC_{20}$ appear in the intermediate frequency range of 10–15 THz. This phenomenon can be attributed to the fact that the characteristic vibrational frequency of an atom is co-determined by its atomic mass and the binding force acting on it. A lower atomic mass and stronger binding give rise to a higher vibrational frequency. Among all dopant elements, Li has the lowest atomic mass; this mass effect significantly elevates its fundamental vibrational frequency, shifting its characteristic vibrational modes into the intermediate frequency range. Mg and Na, located in the same period of the periodic table, have similar atomic masses; however, Mg exhibits divalent charge transfer and donates a much greater amount of charge to the carbon framework than monovalent Na. This difference in charge transfer magnitude is

directly corroborated by the results of the Bader charge analysis. The greater charge transfer magnitude gives rise to stronger electrostatic interactions and enhanced binding between Mg and the carbon cage framework. This enhanced binding strength compensates for the mass effect, which eventually shifts its vibrational frequency into the intermediate frequency range as well. For heavier divalent elements in the same group, such as Sr and Ba, the effect of the larger atomic mass outweighs the enhanced binding strength, such that their characteristic vibrational modes remain in the low-frequency region.

Although the vibrational modes of the endohedral atoms shift to the intermediate-frequency range in $LiC_{20}$ and $MgC_{20}$, their electron–phonon coupling (EPC) constant $\lambda$ and superconducting transition temperature $T_C$ are not significantly enhanced compared with other $XC_{20}$ compounds. This can be explained by the relatively low density of states at the Fermi level $N(E_F)$ of $LiC_{20}$ and $MgC_{20}$ (28.113 and 29.160 states/eV, respectively; Table 4), which fundamentally limits the electronic contribution to EPC, resulting in low overall $\lambda$ values (0.437 for $LiC_{20}$ and 0.376 for $MgC_{20}$) and low $T_C$. This analysis demonstrates that the frequency upshift of endohedral atoms alone is insufficient to enhance superconductivity; strong EPC and high $T_C$ can only be achieved when combined with an optimized density of states at the Fermi level.

Analysis of the Eliashberg spectral function demonstrates that the contribution of the carbon cage framework to electron–phonon coupling is predominantly

concentrated in the mid-to-high frequency region above 10 THz. With the exception of Li and Mg, whose characteristic vibrational modes shift to the intermediate frequency range, the vibrational contributions of all other endohedral dopant atoms reside in the low-frequency region of 0–10 THz. To intuitively reveal the superconducting properties of the materials and the spectral distribution of electron–phonon coupling, we project the electron–phonon coupling constant $\lambda$ of each vibrational mode onto the phonon dispersion spectrum (Figure 4). The color scale from black to red indicates a progressively increasing contribution of the corresponding phonon mode to the electron–phonon coupling. On this basis, we further analyze the frequency range where the electron–phonon coupling contributes dominantly to the superconducting transition temperature. By comparing the spectral distributions of $\lambda$ across different systems, we find that in systems with a higher superconducting transition temperature, the electron–phonon coupling strength is significantly enhanced in the low-frequency phonon region. Quantitatively, for $ClC_{20}$ and $PC_{20}$ with the highest $T_C$, the contribution of low-frequency modes (0–10 THz) to the total $\lambda$ reaches 57.86% and 64.15%, respectively; while for $LiC_{20}$ and $MgC_{20}$ with low $T_C$, this proportion drops to 12.91% and 13.38%, respectively. This quantitative result confirms that, within the scope of the present systems, the effective participation of low-frequency vibrational modes induced by endohedral atoms in the EPC process is a key factor for achieving strong electron–phonon interaction and high $T_C$. In contrast, in systems with a lower superconducting transition temperature, the

distribution of $\lambda$ with frequency is relatively flat, the coupling strength in the low-frequency region is weak, and there are very few red-projected regions on the dispersion spectrum.

Consistent with the partial charge density analysis presented in the previous section, the electronic states at the Fermi level are predominantly localized at the shared carbon sites where three six-membered rings intersect on the carbon cage framework. In the $PC_{20}$ and $ClC_{20}$ systems, which exhibit the highest superconducting transition temperatures, the Fermi level features both a higher electronic density of states and more pronounced spatial localization of the corresponding electronic states. From the perspective of the microscopic coupling mechanism, $N(E_F)$ and the spatial localization degree of Fermi-level electron wavefunctions together constitute the electronic baseline of electron–phonon coupling. Specifically, $N(E_F)$ provides the quantitative basis by defining the number of electronic states at the Fermi surface available for electron–phonon scattering, while the spatial localization of electrons modulates the overlap efficiency between electron wavefunctions and the lattice vibrational displacement field, and thus influences the intrinsic matrix element strength of EPC. These two factors act in a synergistic manner: a combination of higher $N(E_F)$ and more pronounced electron localization can improve the electronic-side coupling strength from both the state count and interaction efficiency aspects. This physical picture is consistent with the trends observed in our ELF maps, partial charge density distributions and total $\lambda$ values across the studied systems.

The $T_C$ behavior of $SrC_{20}$ further supports this synergistic trend. This system exhibits the highest $N(E_F)$ (43.064 states/eV) among all the investigated compounds; however, it can be visually observed from the partial charge density distributions that the spatial localization of Fermi-level electrons in $SrC_{20}$ is notably weaker than that in $PC_{20}$ and $ClC_{20}$. A single advantage in state density is insufficient to yield the strongest EPC, which explains why its total $\lambda$ and $T_C$ are both lower than those of $PC_{20}$ and $ClC_{20}$. This observation also indicates that no single electronic parameter can fully determine the superconducting performance, and the synergistic matching between the number of electronic states and their spatial distribution is the key.

In summary, this section calculates the superconducting properties of ten ambient-pressure metallic carbon cage compounds using first-principles calculations combined with the McMillan equation, confirms their dynamical stability at ambient pressure, analyzes the frequency-partitioned characteristics of phonon states and the special vibrational behavior of $LiC_{20}$ and $MgC_{20}$, and reveals that the electron-phonon coupling strength and superconducting transition temperature are jointly determined by the concerted contribution of low-frequency endohedral modes and mid-to-high-frequency carbon cage modes, as well as the synergistic effect of Fermi-level density of states and electronic spatial localization.

## 4.Conclusions

We perform systematic first-principles calculations within the density functional theory framework to investigate the structural stability, electronic structure, and superconducting properties of endohedrally doped $XC_{20}$ compounds based on the $C_{20}$ carbon cage covalent framework. This work focuses on elucidating the underlying mechanism for the remarkable differences in EPC strength and superconducting transition temperature $T_C$ induced by different endohedral atoms in the identical carbon cage skeleton. Our results show that differences in electronegativity and valence state of endohedral atoms induce charge transfer of varying magnitudes. All endohedral atoms donate electrons to the carbon cage except Cl, which withdraws electrons due to its high electronegativity. This charge transfer directly gives rise to distinct densities of states at the Fermi level $N(E_F)$ among different systems. The electronic states at the Fermi level originate mainly from carbon 2p orbitals, and localize at the carbon sites where three six-membered rings intersect on the cage. The degree of spatial localization of Fermi-level electrons varies across systems. Systems with higher $N(E_F)$, such as $PC_{20}$ and $ClC_{20}$, exhibit more pronounced electron spatial localization. The $N(E_F)$ and the spatial localization of electron wavefunctions jointly determine the electronic baseline strength of EPC. Higher $N(E_F)$ provides more electronic states available for coupling. Stronger spatial localization increases the spatial overlap between Fermi-level electron wavefunctions and the phonon

displacement fields of the carbon cage, enhancing the strength of EPC eigenmatrix elements. Both factors contribute to the coupling efficiency on the electronic side. On the phonon side, the phonon spectra of all systems exhibit clear frequency zoning features. The mid-to-high frequency range above 10 THz arises from intrinsic lattice vibrations of the carbon cage framework. The low-frequency range of 0–10 THz corresponds mainly to localized vibrations of endohedral atoms. The characteristic vibrational frequency of endohedral atoms is determined by both their atomic mass and the binding strength with the carbon cage. Li has the lowest atomic mass, and Mg shows stronger electrostatic binding due to divalent charge transfer. Their characteristic vibrational modes both upshift to the mid-frequency range of 10–15 THz. For heavy atoms such as Sr and Ba, the mass effect dominates, and their vibrational modes remain in the low-frequency range. Analysis of the Eliashberg spectral function $\alpha^2F(\omega)$ reveals that low-frequency endohedral vibrational modes contribute significantly more to the total EPC strength than mid-to-high frequency intrinsic cage vibrations. Systems with higher $T_C$ show a more prominent EPC enhancement effect in the low-frequency range. A single advantageous factor is insufficient to achieve high $T_C$. The synergistic matching between electronic structure and phonon spectrum is the core origin of performance differences. In $LiC_{20}$ and $MgC_{20}$, although endohedral vibrational frequencies are upshifted, the low $N(E_F)$ and the loss of strong coupling from low-frequency vibrational modes result in weak EPC and low $T_C$. $SrC_{20}$ possesses the highest $N(E_F)$ among all systems, but its electron

spatial localization is relatively weak. Hence its $T_C$ is lower than those of $PC_{20}$ and $ClC_{20}$. $PC_{20}$ and $ClC_{20}$ combine high $N(E_F)$, pronounced electron spatial localization, and effective participation of low-frequency endohedral vibrational modes in EPC. The synergistic effect of multiple factors yields the strongest EPC and the highest $T_C$. This work reveals the modulation mechanism of endohedral atoms on the superconducting properties of carbon cage systems, and provides theoretical support for the design of ambient-pressure carbon-based superconducting materials.

## Data availability

The data that support the findings of this study are available within the paper are available from the corresponding author upon reasonable request.

## Conflicts of interest

There are no conflicts of interest to declare.

## Contribution statement

Pei-Yun Xu : Methodology, Formal analysis, Investigation, Writing - Original Draft

Qi-Jun Liu: Conceptualization, Project administration, Writing - Review & Editing, Funding acquisition

## Acknowledgements

This work has been supported by the Fundamental Research Funds for the Central Universities (Nos. 2682025ZTPY013 and 2682026ZTPY017), and the High-performance Computing Platform of Southwest Jiaotong University.

References

[1] Poole, R. 1988 Science **240** 146-148.

[2] Gambino, D., Di Eugenio, N., Byggmästar, J., Klarbring, J., Torsello, D., Djurabekova, F., and Laviano, F. 2026 npj Quantum Materials **11** 41.

[3] Kim, S., Chen, X., Fitzhugh, W. and Li, X. 2018 Physical review letters 121 157001.

[4] Liu, Z., Li, J., Zurek, E., Zhuang, Q., Liu, Y., Yue, J., Guo, S., Zhang, A., Chi, Z., Huang, X., and Cui, T. 2024 Physical Review B **109** L180501.

[5] Chen, S., Guo, J., Wang, Y., Wu, X., Chen, W., Huang, X., and Cui 2024 Physical Review B **109** 224510.

[6] Zhang, J., Zhang, X., He, B., and Xu, L. 2026 Physical Review B **113** 094525.

[7] He, X. L., Zhao, W., Xie, Y., Hermann, A., Hemley, R. J., Liu, H., and Ma, Y. 2024 Proceedings of the National Academy of Sciences **121** e2401840121.

[8] Tao, Y.L., Zeng, W., Fan, D.H., Liu, Z.T. and Liu, Q.J. 2025 Crystal Growth & Design **25** 9513.

[9] Zhao, S., Gao, J., Fan, D.H., Liu, Z.T. and Liu, Q.J. 2026 Chinese Journal of Physics **103** 147.

[10] Du, H., and Guo, W. 2022 Journal of Physics: Condensed Matter **34** 235702.

[11] Zhao, X., Huang, Y., Ma, S., Song, H., Cao, Y., Jiang, H., Huang, Y. and Cui, T. 2025 Advanced Science **12** 2409092.

[12] Zhang, M., Pei, C., Zhu, B., Wang, Q., Wu, J. and Qi, Y. 2025 Physical Review B **112** 184108.

[13] Fleming, R.M., Ramirez, A.P., Rosseinsky, M.J., Murphy, D.W., Haddon, R.C., Zahurak, S.M. and Makhija, A.V. 1991 Nature **352** 787.

[14] Yokoya, T., Nakamura, T., Matsushita, T., Muro, T., Takano, Y., Nagao, M., Takenouchi, T., Kawarada, H. and Oguchi, T. 2005 Nature **438** 647.

[15] Mareš, J., Hubík, P., Krištofik, J. and Nesládek, M. 2008 Science and Technology of Advanced Materials **9** 044101.

[16] Ma, G., Wang, Y., Wang, Z., Nakamoto, Y., Shimizu, K., Liu, G., Zhou, M., Wang, H., Gao, P. and Ma, Y. 2025 Physical Review Letters **135** 166003.

[17] Zinni, J., Camerano, L., Speyer, L., Cahen, S., El Hajj, I., Bolmont, M., Medjahdi, G., Lagrange, P., Lamura, G., Profeta, G. and Hérold, C. 2024 Carbon **230** 119652.

[18] Han, Y.L., Jiang, K.Y., Wang, B.T., Zhang, P. and Lu, H.Y. 2024 Physical Review B **110** 104504.

[19] Qiu, Z.Y., Li, W.G., Fan, D.H., Liu, Z.T. and Liu, Q.J. 2026 Crystal Growth & Design **26** 5753.

[20] Wang, J.N., Yan, X.W. and Gao, M. 2021 Physical Review B **103** 14451 5.

[21] Zhu, L., Liu, H., Somayazulu, M., Meng, Y., Guńka, P.A., Shiell, T.B., Kenney-Benson, C., Chariton, S., Prakapenka, V.B., Yoon, H. and Horn, J.A.

2023 Physical Review Research **5** 013012.

[22] Zhang, P., Li, X., Yang, X., Wang, H., Yao, Y. and Liu, H. 2022 Physical Review B **105** 094503.

[23] Di Cataldo, S., Qulaghasi, S., Bachelet, G.B. and Boeri, L. 2022 Physical Review B **105** 064516.

[24] Giannozzi, P., Andreussi, O., Brumme, T., Bunau, O., Buongiorno Nardelli, M., Calandra, M., Car, R., Cavazzoni, C., Ceresoli, D., Cococcioni, M. and Colonna, N. 2017 Journal of physics: Condensed matter **29** 465901.

[25] Perdew, J.P. and Yue, W. 1986 Physical review B **33** 8800.

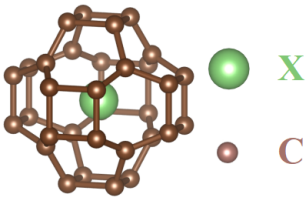
[26] Perdew, J.P. and Wang, Y. 1992 Physical Review B **46** 12947.

[27] Perdew, J.P., Burke, K. and Ernzerhof, M., 1996 Physical review letters **77** 3865.

[28] Vanderbilt, D. 1990 Physical review B **41** 7892.

[29] Filipe J. Ribeiro, Paul Tangney, Steven G. Louie and Marvin L. 2006 Cohen Physical Review B **74** 172101

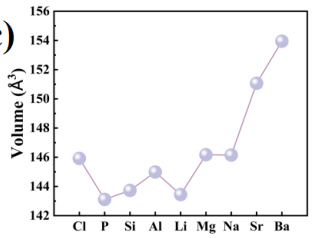
(a)




(b)

| $LiC_{20}$ | $NaC_{20}$ | $MgC_{20}$ | $AlC_{20}$ | $SiC_{20}$ |
|---|---|---|---|---|
| 4.723 K | 12.538 K | 2.288 K | 1.814 K | 8.406 K |
| $PC_{20}$ | $ClC_{20}$ | $SrC_{20}$ | $BaC_{20}$ | $C_{20}$ |
| 19.836 K | 29.572 K | 16.159 K | 0.214 K | 9.921 K |

(c)




(d)

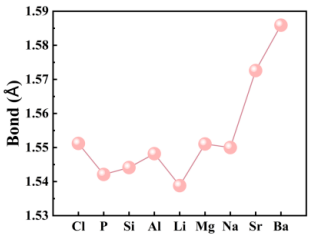
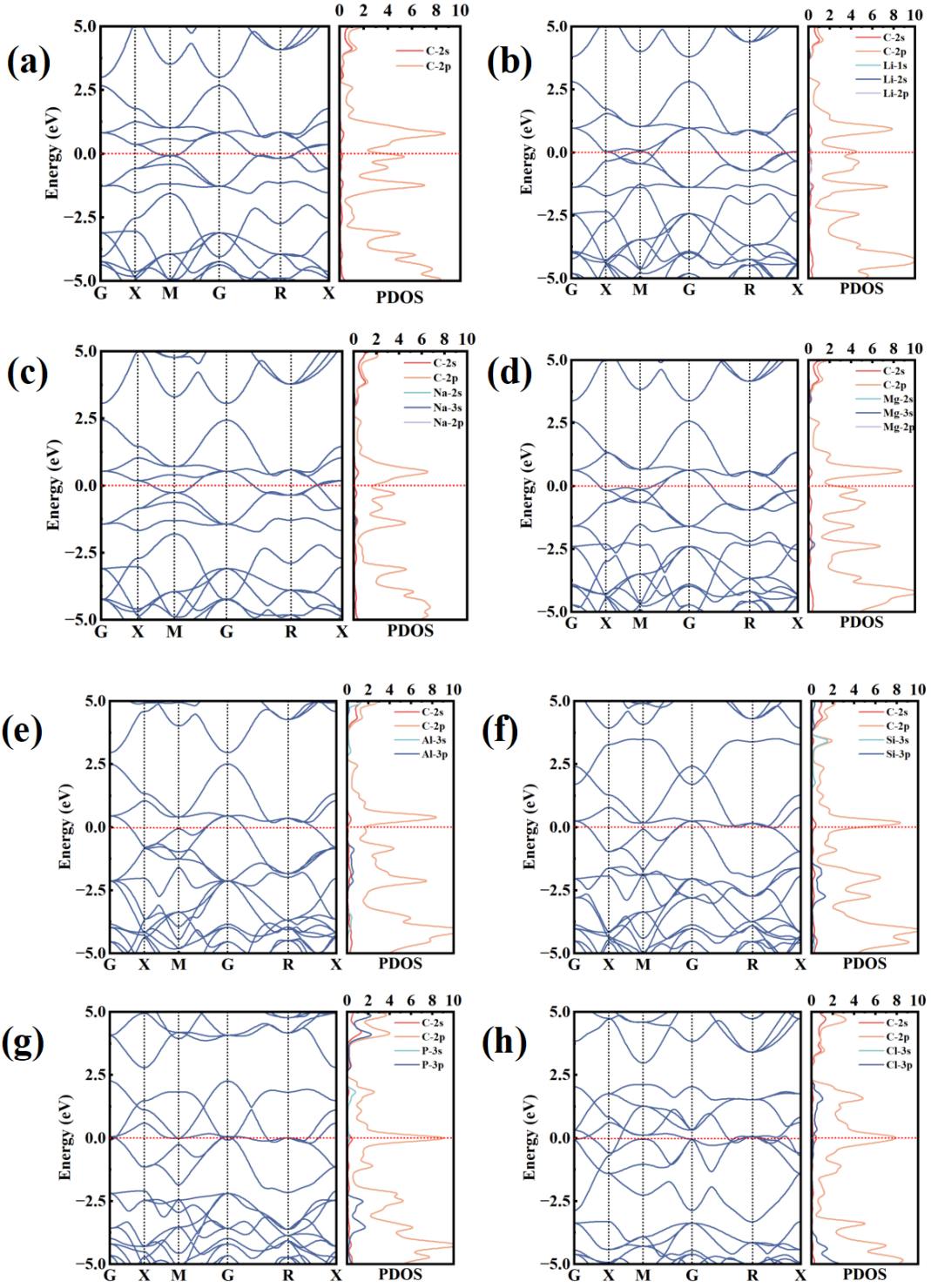



Figure 1. (a) Structural diagram of $XC_{20}$, where the green spheres represent the doped X atoms and the brown spheres represent the C atoms; (b) Superconducting transition temperatures of $XC_{20}$; (c) Variation of the unit cell volume of the $XC_{20}$ system as a function of atomic radius; (d) Variation of the average C–C bond length in the $XC_{20}$ structure as a function of the atomic radius.


(a)
(b)
(c)
(d)
(e)
(f)
(g)
(h)
Energy (eV)
5.0
2.5
0.0
−2.5
−5.0
G X M G R X
PDOS
0 2 4 6 8 10
C-2s
C-2p
Li-1s
Li-2s
Li-2p
Na-2s
Na-3s
Na-2p
Mg-2s
Mg-3s
Mg-2p
Al-3s
Al-3p
Si-3s
Si-3p
P-3s
P-3p
Cl-3s
Cl-3p

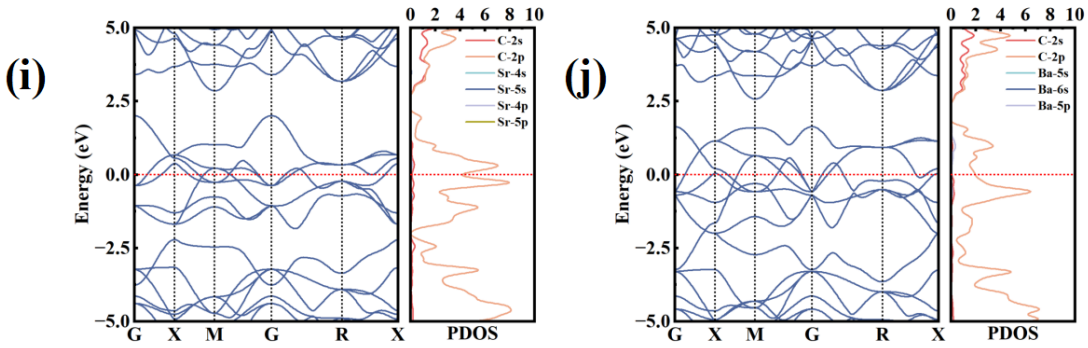
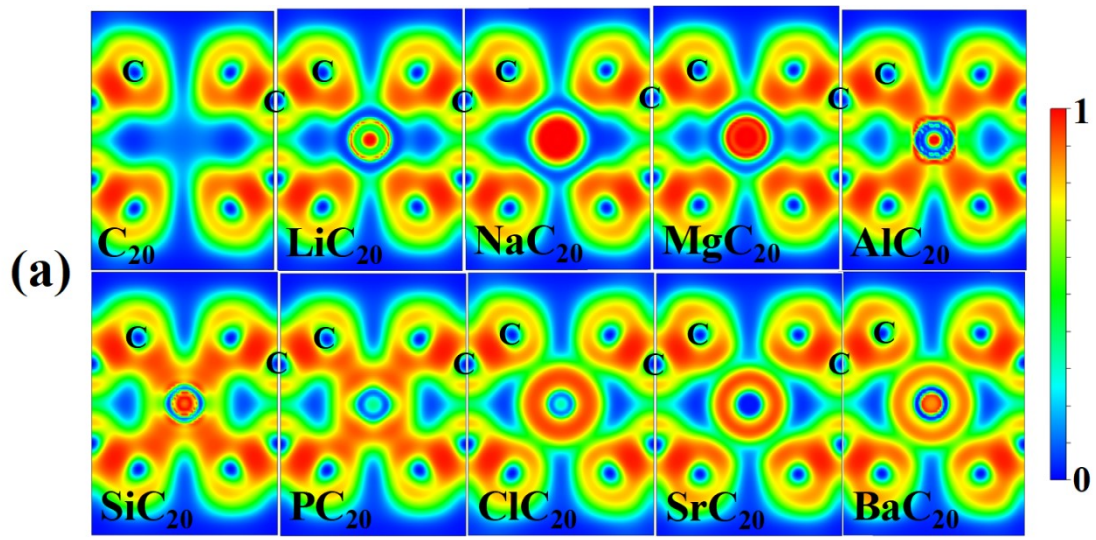
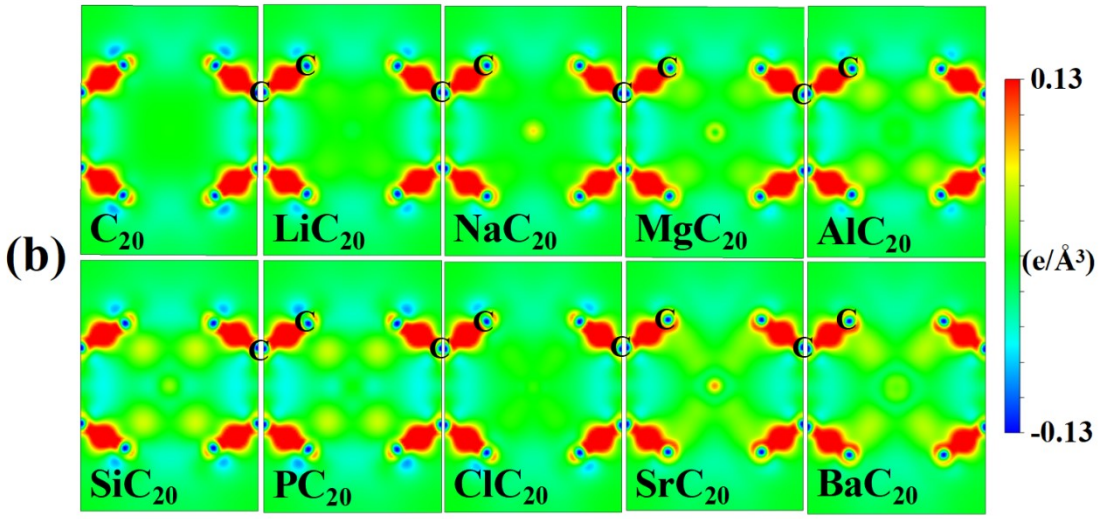



Figure 2. The band structures and partial density of states of (a) $C_{20}$, (b) $LiC_{20}$, (c) $NaC_{20}$, (d) $MgC_{20}$, (e) $AlC_{20}$, (f) $SiC_{20}$, (g) $PC_{20}$, (h) $ClC_{20}$, (i) $SrC_{20}$, (j) $BaC_{20}$..


(a)
C
C20
LiC20
NaC20
MgC20
AlC20
SiC20
PC20
ClC20
SrC20
BaC20
1
0


(b)
C
C20
LiC20
NaC20
MgC20
AlC20
SiC20
PC20
ClC20
SrC20
BaC20
0.13
(e/Å3)
-0.13

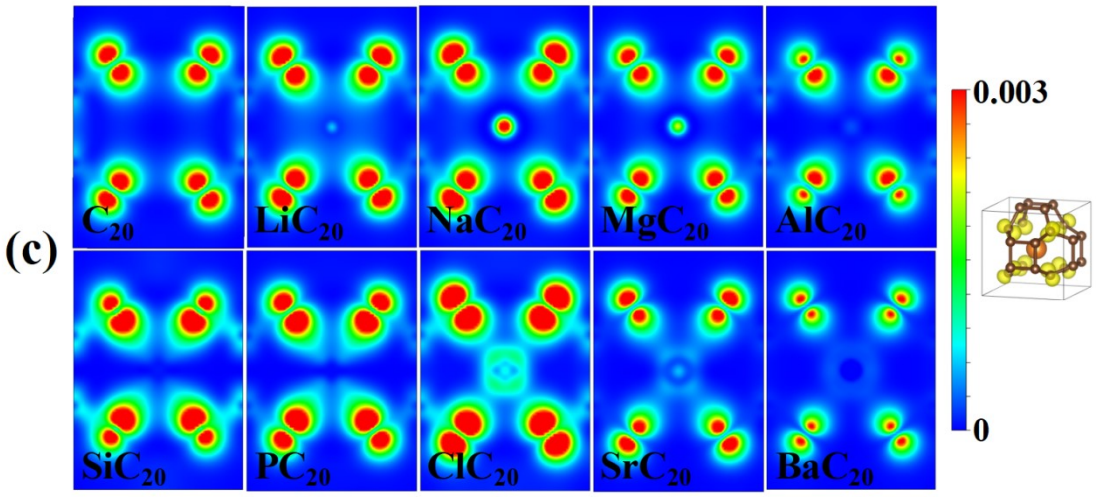

(c)
C20
LiC20
NaC20
MgC20
AlC20
SiC20
PC20
ClC20
SrC20
BaC20
0.003
0

Figure. 3. (a) Charge density map of the $XC_{20}$ system. (b) Differential charge density map of the $XC_{20}$ system. (c) Partial charge density slice and 3D isosurface plots of the $XC_{20}$ system.

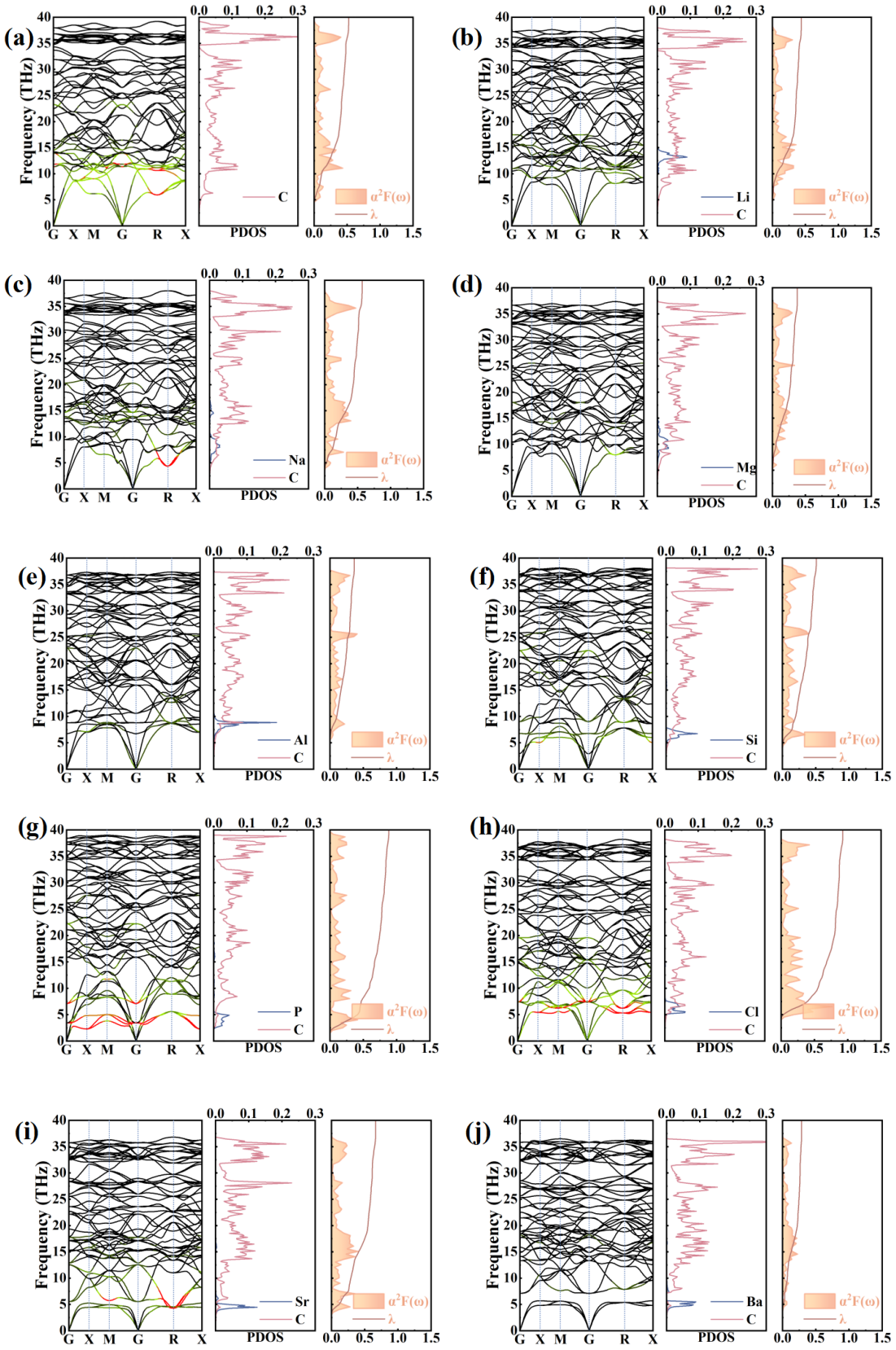

(a)
(b)
(c)
(d)
(e)
(f)
(g)
(h)
(i)
(j)
Frequency (THz)
G X M G R X
PDOS
C
Li
Na
Mg
Al
Si
P
Cl
Sr
Ba
α²F(ω)
λ

Figure 4. The phonon dispersion, phonon density of states, Eliashberg spectral function $\alpha^2F(\omega)$, and electron-phonon coupling constant $\lambda$ for (a) $C_{20}$, (b) $LiC_{20}$, (c) $NaC_{20}$, (d) $MgC_{20}$, (e) $AlC_{20}$, (f) $SiC_{20}$, (g) $PC_{20}$, (h) $ClC_{20}$, (i) $SrC_{20}$, (j) $BaC_{20}$

Table 1 Formation enthalpies of $XC_{20}$

| | $LiC_{20}$ | $NaC_{20}$ | $MgC_{20}$ | $AlC_{20}$ | $SiC_{20}$ | $PC_{20}$ | $ClC_{20}$ | $SrC_{20}$ | $BaC_{20}$ |
|---|---|---|---|---|---|---|---|---|---|
| Formation enthalpies (eV/atom) | 0.666 | 0.752 | 0.674 | 0.615 | 0.612 | 0.638 | 0.745 | 0.815 | 0.883 |

Table 2 Crystallographic parameters of $XC_{20}$.

| | $C_1$ (Å) | $C_2$ (Å) | $C_A$ (Å) | Volume (Å$^3$) |
|---|---|---|---|---|
| $LiC_{20}$ | 1.583 | 1.494 | 1.539 | 143.443 |
| $NaC_{20}$ | 1.604 | 1.496 | 1.550 | 146.149 |
| $MgC_{20}$ | 1.601 | 1.501 | 1.551 | 146.173 |
| $AlC_{20}$ | 1.595 | 1.501 | 1.548 | 144.987 |
| $SiC_{20}$ | 1.589 | 1.499 | 1.544 | 143.729 |
| $PC_{20}$ | 1.588 | 1.496 | 1.542 | 143.110 |
| $ClC_{20}$ | 1.609 | 1.493 | 1.551 | 145.919 |
| $SrC_{20}$ | 1.640 | 1.505 | 1.573 | 151.064 |
| $BaC_{20}$ | 1.661 | 1.510 | 1.586 | 153.944 |

Table 3 Bader charge of X atoms in $XC_{20}$ compounds, where + denotes net electron gain and - denotes net electron loss.

| | $LiC_{20}$ (Li) | $NaC_{20}$ (Na) | $MgC_{20}$ (Mg) | $AlC_{20}$ (Al) | $SiC_{20}$ (Si) | $PC_{20}$ (P) | $ClC_{20}$ (Cl) | $SrC_{20}$ (Sr) | $BaC_{20}$ (Ba) |
|---|---|---|---|---|---|---|---|---|---|
| Bader(X) (e) | -0.821 | -0.765 | -1.568 | -2.920 | -3.885 | -0.594 | 0.121 | -1.236 | -1.265 |

Table 4. The density of states at the Fermi level $N(E_F)$, the average EPC parameter $\lambda$, the logarithmic average frequency $\omega_{log}$, and the superconducting transition temperature $T_C$ of $XC_{20}$ and $C_{20}$.

| Compounds | $N(E_F)$ ( states / eV) | $\omega_{log}$ (K) | $\lambda$ | $T_C$ (K) $\mu^*$=0.1 | $T_C$ (K) $\mu^*$=0.11 |
|---|---|---|---|---|---|
| $LiC_{20}$ | 28.113 | 708.038 | 0.437 | 4.7 | 4.5 |
| $NaC_{20}$ | 37.520 | 651.452 | 0.568 | 12.5 | 11.5 |
| $MgC_{20}$ | 29.160 | 785.947 | 0.376 | 2.3 | 1.9 |
| $AlC_{20}$ | 27.130 | 757.931 | 0.365 | 1.8 | 1,6 |
| $SiC_{20}$ | 32.015 | 653.613 | 0.507 | 8.4 | 7.2 |
| $PC_{20}$ | 31.713 | 346.723 | 0.888 | 19.8 | 18.7 |
| $ClC_{20}$ | 40.640 | 482.111 | 0.924 | 29.6 | 28.0 |
| $SrC_{20}$ | 43.064 | 523.55 | 0.668 | 16.2 | 14.8 |
| $BaC_{20}$ | 24.641 | 685.941 | 0.288 | 0.2 | 0.1 |
| C20 | 33.131 | 676.892 | 0.525 | 9.9 | 9.4 |